Nonreciprocal Light Propagation in a Silicon Photonic Circuit

Liang Feng, *et al.*

Science **333**, 729 (2011);
DOI: 10.1126/science.1206038

References and Notes

1. N. J. White, *Science* **320**, 330 (2008).
2. N. J. White, P. L. Olliaro, *Parasitol. Today* **12**, 399 (1996).
3. H. Noedl *et al.*, *N. Engl. J. Med.* **359**, 2619 (2008).
4. M. Bonnet *et al.*, *Malar. J.* **8**, 192 (2009).
5. A. M. Dondorp *et al.*, *N. Engl. J. Med.* **361**, 455 (2009).
6. C. R. Chong, X. Chen, L. Shi, J. O. Liu, D. J. Sullivan Jr., *Nat. Chem. Biol.* **2**, 415 (2006).
7. J. L. Weisman *et al.*, *Chem. Biol. Drug Des.* **67**, 409 (2006).
8. N. Kato *et al.*, *Nat. Chem. Biol.* **4**, 347 (2008).
9. J. Yuan *et al.*, *Nat. Chem. Biol.* **5**, 765 (2009).
10. W. A. Guiguemde *et al.*, *Nature* **465**, 311 (2010).
11. F. J. Gamo *et al.*, *Nature* **465**, 305 (2010).
12. M. Rottmann *et al.*, *Science* **329**, 1175 (2010).
13. R. Huang *et al.*, *Sci. Transl. Med.* **3**, ps16 (2011).
14. J. Inglese *et al.*, *Proc. Natl. Acad. Sci. U.S.A.* **103**, 11473 (2006).
15. L. K. Basco, J. Le Bras, *Am. J. Trop. Med. Hyg.* **49**, 301 (1993).
16. A. Brockman *et al.*, *Trans. R. Soc. Trop. Med. Hyg.* **94**, 537 (2000).
17. J. Mu *et al.*, *Nat. Genet.* **42**, 268 (2010).
18. J. Seed *et al.*, *Crit. Rev. Toxicol.* **35**, 663 (2005).
19. R. Huang *et al.*, *Chem. Res. Toxicol.* **21**, 659 (2008).
20. P. K. Rathod, T. McErlean, P. C. Lee, *Proc. Natl. Acad. Sci. U.S.A.* **94**, 9389 (1997).
21. J. C. Wootton *et al.*, *Nature* **418**, 320 (2002).
22. M. Randić, *J. Chem. Inf. Comput. Sci.* **37**, 672 (1997).
23. D. A. Fidock *et al.*, *Mol. Cell* **6**, 861 (2000).
24. M. T. Ferdig *et al.*, *Mol. Microbiol.* **52**, 985 (2004).
25. J. M. Sá *et al.*, *Proc. Natl. Acad. Sci. U.S.A.* **106**, 18883 (2009).
26. B. Lell, P. G. Kremsner, *Antimicrob. Agents Chemother.* **46**, 2315 (2002).
27. O. J. Kazzim, O. M. Adegbolagun, O. Osho, C. I. Anumudu, *Ann. Trop. Med. Parasitol.* **100**, 579 (2006).
28. P. Gershon, R. E. Howells, *Trans. R. Soc. Trop. Med. Hyg.* **80**, 753 (1986).
29. M. Mungthin *et al.*, *Am. J. Trop. Med. Hyg.* **83**, 1005 (2010).
30. S. J. Foote *et al.*, *Nature* **345**, 255 (1990).
31. A. F. Cowman, S. Karcz, D. Galatis, J. G. Culvenor, *J. Cell Biol.* **113**, 1033 (1991).
32. D. E. Kyle, W. K. Milhous, R. N. Rossan, *Am. J. Trop. Med. Hyg.* **48**, 126 (1993).
33. A. Sowunmi, *Ann. Trop. Med. Parasitol.* **97**, 103 (2003).
34. N. Singh, S. K. Puri, *Acta Trop.* **77**, 185 (2000).
35. S. J. Burgess *et al.*, *J. Med. Chem.* **53**, 6477 (2010).
36. J. J. Patel *et al.*, *Mol. Microbiol.* **78**, 770 (2010).
37. T. E. Wellems, *Nat. Med.* **10**, 1169 (2004).
38. K. Hayton, X. Z. Su, *Curr. Genet.* **54**, 223 (2008).
39. S. J. Billups, B. L. Carter, *Ann. Pharmacother.* **32**, 659 (1998).

Acknowledgments: We thank P. Shinn and D. Van Leer for compound management, J. Wichterman for assay assistance, R. Eastman and C. O'Brien for comments on the manuscript, and NIAID intramural editor B. R. Marshall for assistance. The raw data from our chemical screening has been deposited at PubChem with accession no. 504749 (http://pubchem.ncbi.nlm.nih.gov/assay/assay.cgi?aid=504749). Because all authors except D.A.F. are government employees and this is a government work, the work is in the public domain in the United States. Notwithstanding any other agreements, the NIH reserves the right to provide the work to PubMedCentral for display and use by the public, and PubMedCentral may tag or modify the work consistent with its customary practices. Rights outside of the United States can be established subject to a government use license. **Funding:** This work was supported by the Intramural Research Program of the Division of Intramural Research at the National Institute of Allergy and Infectious Diseases (NIAID), the National Human Genome Research Institute, and the Director's Challenge Award Program, all at NIH. Funding for the studies from D.A.F. was provided by R01 AI50234 and the Burroughs Wellcome Fund. **Author contributions:** J.Y. performed quantitative high-throughput screening, parasite culture, and data analysis; K.C.-C.C. and R.G. carried out quantitative high-throughput screening and data analysis; R.L.J. and R.H. performed data analysis and writing; S.P. performed in vivo tests of drug combinations; A.L. performed isobologram analyses; R.G. performed the chemical library; D.A.F. transfected parasites and assisted with writing; T.E.W. provided progeny and writing; C.P.A. and J.I. carried out project planning, support, and writing; and X.-z.S. provided project conception, data analysis, and writing. **Competing interests:** The authors declare that they do not have any competing financial interests.

Supporting Online Material

www.sciencemag.org/cgi/content/full/333/6043/724/DC1
Materials and Methods
SOM Text
Figs S1 to S3
Tables S1 to S16
References

7 March 2011; accepted 13 June 2011
10.1126/science.1205216

Nonreciprocal Light Propagation in a Silicon Photonic Circuit

Liang Feng,[1,2,4]*† Maurice Ayache,[3]* Jingqing Huang,[1,4]* Ye-Long Xu,[2] Ming-Hui Lu,[2] Yan-Feng Chen,[2]† Yeshaiahu Fainman,[3] Axel Scherer[1,4]†

Optical communications and computing require on-chip nonreciprocal light propagation to isolate and stabilize different chip-scale optical components. We have designed and fabricated a metallic-silicon waveguide system in which the optical potential is modulated along the length of the waveguide such that nonreciprocal light propagation is obtained on a silicon photonic chip. Nonreciprocal light transport and one-way photonic mode conversion are demonstrated at the wavelength of 1.55 micrometers in both simulations and experiments. Our system is compatible with conventional complementary metal-oxide-semiconductor processing, providing a way to chip-scale optical isolators for optical communications and computing.

An example of nonreciprocal physical response, associated with the breaking of time-reversal symmetry, is the electrical diode (*1*). Stimulated by the vast application of this one-way propagation of electric current, considerable effort has been dedicated to the study of nonreciprocal propagation of light. The breaking of time-reversal symmetry of light is typically achieved with magneto-optical materials that introduce a set of antisymmetric off-diagonal dielectric tensor elements (*2*–*4*) or by involving nonlinear optical activities (*5*, *6*). However, practical applications of these approaches are limited for the rapidly growing field of silicon (Si) photonics because of their incompatibility with conventional complementary metal-oxide-semiconductor (CMOS) processing. Si optical chips have demonstrated integrated capabilities of generating (*7*–*11*), modulating (*12*), processing (*13*) and detecting (*14*) light signals for next-generation optical communications but require on-chip nonreciprocal light propagation to enable optical isolation in Si photonics.

Parity-time (PT) symmetry is crucial in quantum mechanics. In contrast to conventional quantum mechanics, it has been proposed that non-Hermitian Hamiltonians where $\hat{H}^{+} \neq \hat{H}$ can still have an entirely real spectrum with respect to the PT symmetry (*15*, *16*). Due to the equivalence between the Schrödinger equation in quantum mechanics and the wave equation in optics, PT symmetry has been studied in the realm of optics with non-Hermitian optical potentials (*17*–*19*). The breaking of PT symmetry has recently been experimentally observed, showing asymmetric characteristics transverse to light propagation above the PT threshold (*20*, *21*). Here, we have designed a Si waveguide integrated with complex optical potentials that have a thresholdless broken PT symmetry along the direction of light propagation, thus creating on-chip nonreciprocal light propagation.

On a Si-on-insulator (SOI) platform, the designed two-mode Si waveguide is 200 nm thick and 800 nm wide, allowing a fundamental symmetric quasi-TE mode with a wave vector of $k_1 = 2.59k_0$ and a higher-order antisymmetric mode with a wave vector of $k_2 = 2k_0$ at the wavelength of 1.55 μm. Periodically arranged optical potentials are implemented in the Si waveguide and occupy half of the waveguide width in the x direction (Fig. 1A). The optical potentials have a complex modulation in their

[1]Department of Electrical Engineering, California Institute of Technology, Pasadena, CA 91125, USA. [2]Nanjing National Laboratory of Microstructures, Nanjing University, Nanjing, Jiangsu 210093, China. [3]Department of Electrical and Computer Engineering, University of California, San Diego, La Jolla, CA 92093, USA. [4]Kavli Nanoscience Institute, California Institute of Technology, Pasadena, CA 91125, USA.

*These authors contributed equally to this work.
†To whom correspondence should be addressed. E-mail: lfeng@caltech.edu (L.F.); yfchen@nju.edu.cn (Y.F.C.); etcher@caltech.edu. (A.S.)

dielectric constants along light propagation in the z direction compared with the Si waveguide background ($\varepsilon_{Si} = 12.11$), as shown in Fig. 1B

$$\Delta\varepsilon = \exp[iq(z - z_0)] \quad (1)$$

where $q = k_1 - k_2$, and z_0 is the starting point of the first modulation region. This complex exponential variation of $\Delta\varepsilon$ along the z direction introduces a one-way wave vector that is intrinsically not reciprocal because its corresponding Fourier transform is one-sided to the guided light inside the Si waveguide. These complex optical potentials are located in phase with each other with a spacing of $2\pi/q$ (or multiples of $2\pi/q$) in between, such that light modulation always remains in phase with and is consistently applied to guided light. We chose the dielectric constant modulation to be completely passive in order to make the experiment easier to perform, meaning that the modulation length of each optical potential is π/q. Therefore, no gain is required to construct these optical potentials. From a quantum mechanics analysis, these optical potentials have a spontaneously broken PT symmetry with a non-Hermitian Hamiltonian $\hat{H}^+(-x, z) \neq \hat{H}(x, z)$ or $\hat{H}^+(x, -z) \neq \hat{H}(x, z)$ (*22*), suggesting noncommutative binary operations to the Hamiltonian $PT\hat{H}^+ \neq \hat{H}PT$. In our system, this is observed as nonreciprocal light propagation through the optical potentials in the Si waveguide.

More intuitively, the introduced one-way wave vector q shifts the incoming photons of the symmetric mode with an additional spatial frequency: $k_1 + q$ for forward propagation and $-k_1 + q$ for backward propagation. The mode transition between the symmetric mode and the antisymmetric mode can happen only when the phase-matching condition is approximately satisfied $\Delta k = \pm(k_1 - k_2) + q \approx 0$, where + and – represent forward and backward propagation, respectively. In our case, for an incoming symmetric mode the phase-matching condition is only valid in the backward direction, supporting a one-way mode conversion from k_1 to k_2 (Fig. 1C). In the modulated regime, the electric field of light is given by

$$E(x, z, t) = A_1(z)E_1(x)e^{i(k_1 z - \omega t)} + A_2(z)E_2(x)e^{i(k_2 z - \omega t)} \quad (2)$$

where $E_{1,2}(x)$ are normalized mode profiles of two different modes, and $A_{1,2}(z)$ are the corresponding normalized amplitudes of two modes, respectively. Assuming a slowly varying approximation, the coupled-mode equations can be expressed as follows:

$$\frac{d}{dz}A_1(z) = iB_1\exp(iqz)A_1(z) + iC_1A_2(z)$$
$$\frac{d}{dz}A_2(z) = iC_2\exp(i2qz)A_1(z) + iB_2\exp(iqz)A_2(z) \quad (3)$$

for forward propagation and

$$\frac{d}{dz}A_1(z) = -iB_1\exp(iqz)A_1(z) - iC_1\exp(i2qz)A_2(z)$$
$$\frac{d}{dz}A_2(z) = -iC_2A_1(z) - iB_2\exp(iqz)A_2(z) \quad (4)$$

for backward propagation, where $B_1 = \frac{1}{2k_1}\frac{\omega^2}{c^2} \times \frac{\int E_1^*(x)E_1(x)dx}{\int|E_1(x)|^2dx}$, $C_1 = \frac{1}{2k_1}\frac{\omega^2}{c^2}\frac{\int E_1^*(x)E_2(x)dx}{\int|E_1(x)|^2dx}$, $C_2 = \frac{1}{2k_2}\frac{\omega^2}{c^2}\frac{\int E_2^*(x)E_1(x)dx}{\int|E_2(x)|^2dx}$, and $B_2 = \frac{1}{2k_2}\frac{\omega^2}{c^2}\frac{\int E_2^*(x)E_2(x)dx}{\int|E_2(x)|^2dx}$.

The mode transition can happen only when the phase-matching condition is satisfied as the exponential term disappears because $\exp(i\Delta kz) = 1$. Therefore, it is evident that with an initial condition of $A_1 = 1$ and $A_2 = 0$, photons from the symmetric mode can be converted to the antisymmetric mode only for backward propagation, whereas A_2 remains 0 for forward propagation, indicating negligible mode conversion. The nonreciprocity of the mode transition here results from the spontaneous breaking of the PT symmetry of guided light by the engineered complex optical potentials. It is worth emphasizing that this nonreciprocal unidirectional mode transition is always valid with any modulation intensity, indicating a completely thresholdless breaking of PT symmetry (*22*), in stark contrast to previous work on threshold PT symmetry breaking (*20*, *21*).

Fully vectorial three-dimensional (3D) finite element method simulations have been performed to validate the proposed nonreciprocal propagation of guided light at the telecom wavelength of 1.55 μm. With a TE-like symmetric incident mode, after forward propagating through the PT optical potentials where $\Delta\varepsilon$ follows the exponential modulation, guided light does not meet any phase-matching condition with the additional wave vector q and therefore retains the same symmetric mode profile. However, for backward propagation, it is evident that the antisymmetric mode is converted from the incoming symmetric mode due to the phase matching with the additional wave vector q, showing a one-way mode transition (Fig. 2A). The nonreciprocal light propagation can also be analytically calculated using the coupled-mode theory from Eqs. 2 to 4 (fig. S1), consistent with the simulated results.

However, the approach so far demonstrated to create the exponentially modulated $\Delta\varepsilon$ (*21*) is difficult to integrate with Si photonics. It is there-

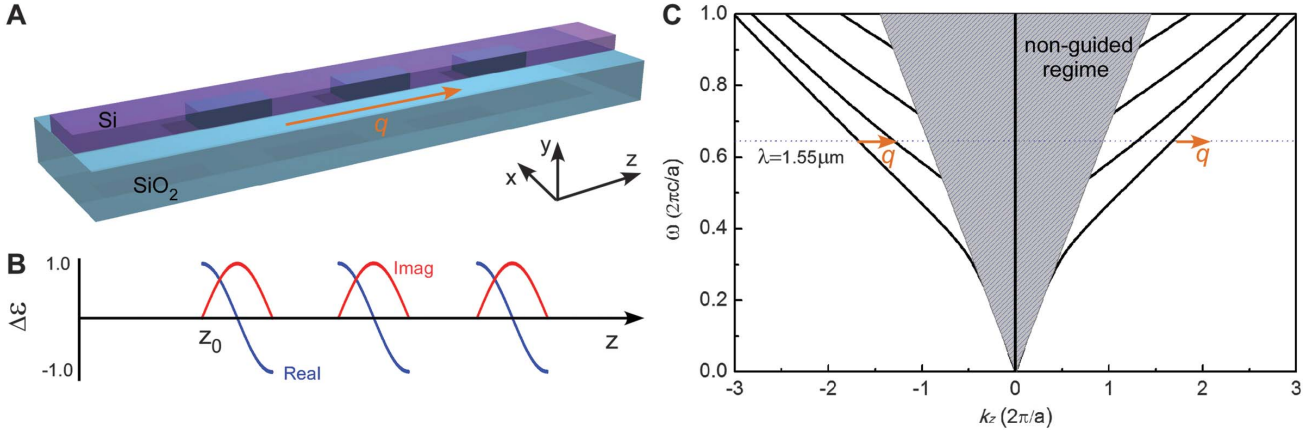

Fig. 1. (**A**) Nonreciprocal light propagation in a Si photonic circuit. Based on a SOI platform, PT optical potentials with exponentially modulated dielectric constants, as depicted in (**B**) where blue and red curves represent the real and imaginary parts of $\Delta\varepsilon$, respectively, are embedded in the Si waveguide to introduce an additional wave vector q to guided light. (**C**) Band diagram for TE-like polarization of the Si waveguide, where the frequency and wave vector are normalized with $a = 1$ μm. At the wavelength of 1.55 μm, if incoming light is a fundamental symmetric mode, one-way mode conversion is only expected for backward propagation where the phase-matching condition is satisfied as indicated by arrows.

fore necessary to design an equivalent guided-mode modulation that at a macroscopic scale mimics the intrinsically microscopic exponential modulation of the PT optical potentials. To simplify fabrication, each complex exponential modulation is separated into two different modulation regions: one providing only the imaginary sinusoidal modulation of the dielectric constant covering one transverse half space (bottom) of the waveguide, and the other creating the real cosine modulation occupying the other transverse half space (top) of the waveguide (Fig. 2B), as follows

$$\Delta\varepsilon_{real} = -\cos[q(z - z_0)]$$
$$\Delta\varepsilon_{imag} = i\sin[q(z - z_0)] \quad (5)$$

Although individual sinusoidal or cosine modulation does not contribute to the breaking of PT symmetry, simultaneous modulations of both cause an equivalent nonreciprocal one-way mode transition. Guided light in different half spaces experiences complementary mode modulation from each other and therefore behaves as if the PT optical potentials do exist. Moreover, to have only the positive $\Delta\varepsilon_{real}$ of the modulations for ease of fabrication, regions of $\Delta\varepsilon_{real}$ are shifted $\pi/2q$ in the z direction: $\Delta\varepsilon_{real} = \sin[q(z - (z_0 + \pi/2q))]$ (Fig. 2C). The resulting one-way mode transition of guided light consequently remains the same.

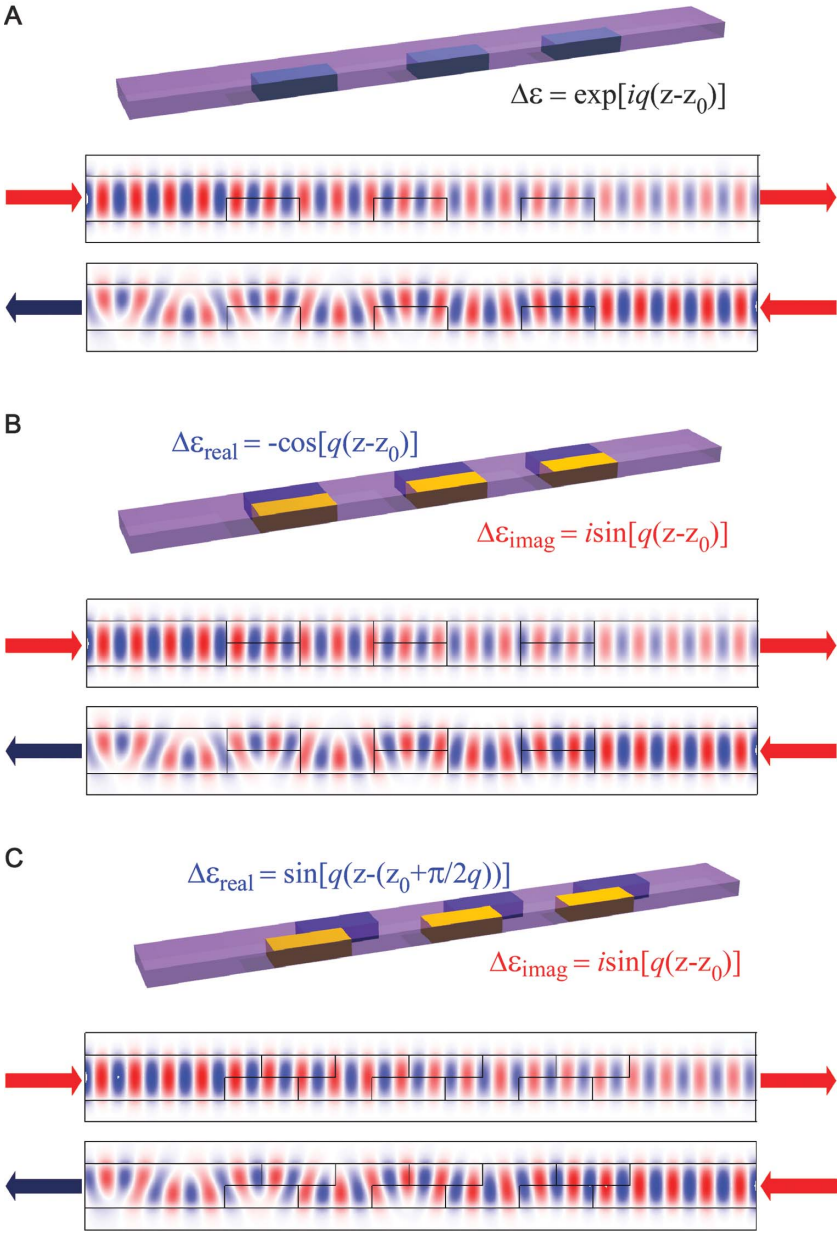

Fig. 2. Evolution of PT optical potentials in the Si waveguide (top) and their corresponding field distributions of E_x for forward (middle) and backward (bottom) propagation with an incoming symmetric mode. (**A**) Original PT optical potentials with exponentially modulated dielectric constant. (**B**) Two different kinds of optical potentials with real cosine and imaginary sinusoidal modulated dielectric constants. (**C**) Optical potentials with the real part modulation in (B) are shifted $\pi/2q$ in the z direction.

Finally, to achieve sinusoidal optical potentials using microscopically homogeneous materials, sinusoidal-shaped structures are adopted on top of the Si waveguide for both real and imaginary modulations to mimic the modulations described in Eq. 5 (Fig. 3A). An 11-nm germanium (Ge)/18-nm chrome (Cr) bilayer structure is applied for the imaginary modulation $\Delta\varepsilon_{imag}$ as guided modes have the same effective indices as $\Delta\varepsilon = i$. For the real modulation $\Delta\varepsilon_{real}$, additional 40-nm Si on top of the original Si waveguide achieves the same effective indices of guided modes as $\Delta\varepsilon = 1$. The length, period, and locations of these sinusoidal shaped structures follow those in Fig. 2C. The designed sinusoidal-shaped structures have almost the same effective indices of the waveguide modes, as if the real and imaginary function-like modulations exist in the waveguide (Fig. 3, B and C), such that the same unidirectional wave vector q can be introduced. Therefore, an equivalent one-way mode transition is realized, as shown in Fig. 3D: Forward propagating light remains in the symmetric profile, whereas mode conversion from the symmetric mode to the antisymmetric mode exists for backward propagation. It is thus evident that our classical waveguide system successfully mimics the quantum effect inherently associated with a broken PT symmetry. Overall, at different steps of the evolution of PT optical potentials from Fig. 2 to Fig. 3, guided light exhibits almost identical phase and intensity for both forward and backward propagation, further proving the equivalence of our classical design to the quantum PT potentials for guided light. To confirm the thresholdless condition of the breaking of PT symmetry in our system, we also designed and simulated different Si and Ge/Cr combinations corresponding to different modulation intensities from $\Delta\varepsilon = 0.25\exp[iq(z - z_0)]$ to $\Delta\varepsilon = 0.75\exp[iq(z - z_0)]$ (fig. S2). Although conversion efficiencies reduce as modulation intensities decrease, one-way mode conversion always exists, indicating that the breaking of PT symmetry in our system is spontaneous without any threshold.

A picture of the fabricated device is shown in Fig. 4A. Nonreciprocal light propagation in the Si waveguide was observed using a near-field scanning optical microscope (*23*). In experiments, a tapered fiber was used to couple light into the waveguide. Although the fundamental symmetric mode is dominant in incidence, there also exists some power coupled to the antisymmetric mode as shown in Fig. 4B. Consistent with simulations, light remains predominantly the fundamental symmetric mode after propagating through the optical potentials for forward propagation. However, the symmetric-mode-dominant incoming light in backward propagation clearly shows mode conversion to the antisymmetric mode

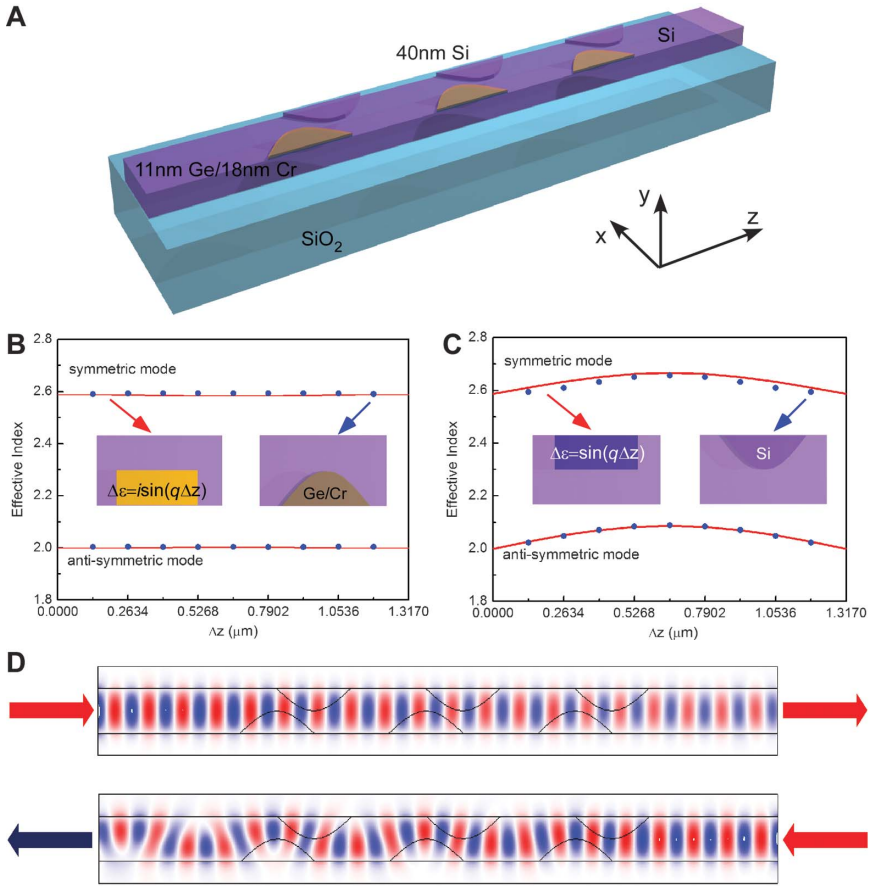

Fig. 3. (**A**) Design of the metallic-Si waveguide to mimic the light modulation of PT optical potentials. (**B**) Effective indices of symmetric and antisymmetric modes with the imaginary part sinusoidal-modulated optical potential (red lines) and the sinusoidal-shaped Ge/Cr bilayer structure (blue dots). (**C**) Modes' effective indices with the real part sinusoidal-modulated optical potential (red lines) and the sinusoidal-shaped Si structure (blue dots). Insets in (B) and (C) show the considered waveguide, and Δz starts from where modulation begins. (**D**) Numerical mappings of E_x for forward (upper) and backward (lower) propagation with an incoming symmetric mode.

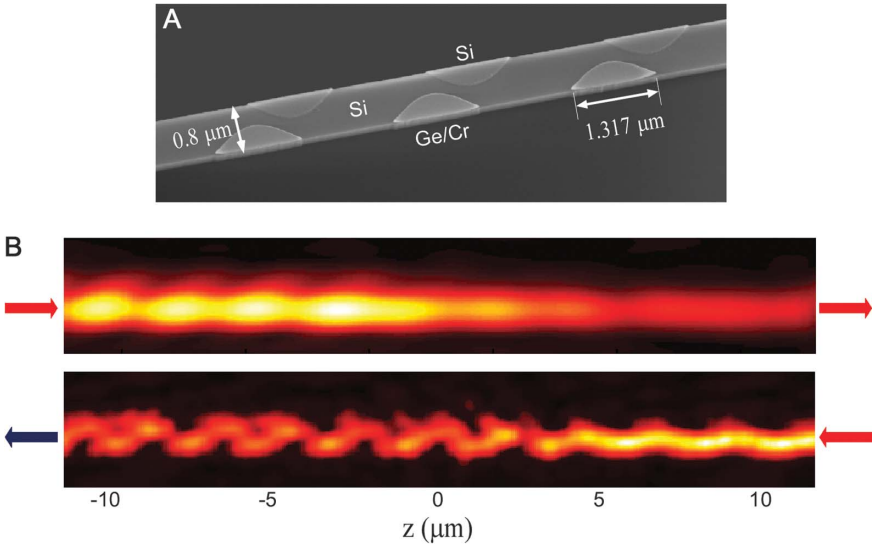

Fig. 4. (**A**) Scanning electron microscope image of the fabricated device. (**B**) Measured near-field amplitude distribution of light in the one-way mode converter for both forward (upper) and backward (lower) light propagation.

after the device. With phase information of guided light simultaneously obtained using our heterodyne system (*22*, *23*), we applied the Fourier transform analysis to the measured field distribution. The results further confirm that the breaking of PT symmetry in our system as the conversion from the symmetric mode to the antisymmetric mode can be observed only in the backward direction (fig. S3). It is therefore evident that one-way mode conversion and nonreciprocal light propagation have been successfully realized in CMOS-compatible Si photonics, paving the way to on-chip optical isolation. Although the insertion loss of about 7 dB is observed through the optical potentials, it can be completely compensated by incorporating gain into the imaginary part modulation of the PT optical potentials in Eqs. 1 and 5. One can easily envision constructing chip-scale isolators by extending the demonstrated nonreciprocal light propagation. The excited antisymmetric mode can be removed in transmitted fields by implementing, next to the PT optical potentials, an optical mode filter that completely reflects the antisymmetric mode but allows the symmetric mode to transmit. Optical isolation with large extinction ratio can be achieved by controlling interference between incidence and reflection.

The nonreciprocal light propagation we have accomplished in a Si photonic circuit is expected to have strong impacts in both fundamental physics and device applications. The feasibility of mimicking complicated quantum phenomena in classical systems promises completely chip-scale optical isolation for rapidly growing Si photonics and optical communications. The proposed one-way system is completely linear and expected to have higher efficiencies and broader operation bandwidths than nonlinear strategies. Analogously the concept of this one-way propagation can be applied to other classical waves, such as sound, as a promising method to drastically increase the rectification efficiency over current nonlinearity-induced isolation (*24*).

References and Notes

1. S. M. Sze, *Semiconductor Devices: Physics and Technology* (Wiley, New York, ed. 2, 2001).
2. J. D. Jackson, *Classical Electrodynamics* (Wiley, New York, ed. 3, 1998).
3. T. Amemiya, K. Abe, T. Tanemura, T. Mizumoto, Y. Nakano, *IEEE J. Quantum Electron.* **46**, 1662 (2010).
4. Z. Wang, Y. Chong, J. D. Joannopoulos, M. Soljačić, *Nature* **461**, 772 (2009).
5. K. Gallo, G. Assanto, K. R. Parameswaran, M. M. Fejer, *Appl. Phys. Lett.* **79**, 314 (2001).
6. Z. Yu, S. Fan, *Nat. Photonics* **3**, 91 (2009).
7. D. Liang, J. E. Bowers, *Nat. Photonics* **4**, 511 (2010).
8. R. Chen *et al.*, *Nat. Photonics* **5**, 170 (2011).
9. O. Painter *et al.*, *Science* **284**, 1819 (1999).
10. M. P. Nezhad *et al.*, *Nat. Photonics* **4**, 395 (2010).
11. X. Sun *et al.*, *Opt. Lett.* **34**, 1345 (2009).
12. M. Hochberg *et al.*, *Nat. Mater.* **5**, 703 (2006).
13. M. A. Foster *et al.*, *Nature* **456**, 81 (2008).
14. J. Michel, J. Liu, L. C. Kimerling, *Nat. Photonics* **4**, 527 (2010).
15. C. M. Bender, S. Boettcher, *Phys. Rev. Lett.* **80**, 5243 (1998).
16. C. M. Bender, *Rep. Prog. Phys.* **70**, 947 (2007).

17. K. G. Makris, R. El-Ganainy, D. N. Christodoulides, Z. H. Musslimani, *Phys. Rev. Lett.* **100**, 103904 (2008).
18. R. El-Ganainy, K. G. Makris, D. N. Christodoulides, Z. H. Musslimani, *Opt. Lett.* **32**, 2632 (2007).
19. Z. H. Musslimani, K. G. Makris, R. El-Ganainy, D. N. Christodoulides, *Phys. Rev. Lett.* **100**, 030402 (2008).
20. A. Guo *et al.*, *Phys. Rev. Lett.* **103**, 093902 (2009).
21. C. E. Rüter *et al.*, *Nat. Phys.* **6**, 192 (2010).
22. Materials and methods are available as supporting material on *Science* Online.
23. M. Abashin *et al.*, *Opt. Express* **14**, 1643 (2006).
24. B. Liang, X. S. Guo, J. Tu, D. Zhang, J. C. Cheng, *Nat. Mater.* **9**, 989 (2010).

Acknowledgments: Support by NSF and NSF ERC Center for Integrated Access Networks grant EEC-0812072, Defense Advanced Research Projects Agency under the Nanoscale Architecture for Coherent Hyperoptical Sources program grant W911NF-07-1-0277, National Basic Research Program of China grant 2007CB613202, National Nature Science Foundation of China grants 50632030 and 10874080, and Nature Science Foundation of Jiangsu Province grant BK2007712. We thank Nanonics, Ltd., for extensive training and support in near-field scanning optical microscopy. M.A. acknowledges support of a Cymer Corp. graduate fellowship.

Supporting Online Material
www.sciencemag.org/cgi/content/full/333/6043/729/DC1
Materials and Methods
Figs. S1 to S3
References

24 March 2011; accepted 27 June 2011
10.1126/science.1206038

A Synthetic Model of the Mn_3Ca Subsite of the Oxygen-Evolving Complex in Photosystem II

Jacob S. Kanady, Emily Y. Tsui, Michael W. Day, Theodor Agapie*

Within photosynthetic organisms, the oxygen-evolving complex (OEC) of photosystem II generates dioxygen from water using a catalytic Mn_4CaO_n cluster (*n* varies with the mechanism and nature of the intermediate). We report here the rational synthesis of a $[Mn_3CaO_4]^{6+}$ cubane that structurally models the trimanganese-calcium–cubane subsite of the OEC. Structural and electrochemical comparison between Mn_3CaO_4 and a related Mn_4O_4 cubane alongside characterization of an intermediate calcium-manganese multinuclear complex reveals potential roles of calcium in facilitating high oxidation states at manganese and in the assembly of the biological cluster.

Biological dioxygen generation occurs at the oxygen-evolving complex (OEC) of photosystem II (PSII) in cyanobacteria and plants (*1*). The active site responsible for this transformation consists of a Mn_4CaO_n cluster (*n* varies with the mechanism and nature of the intermediate) embedded in a large protein complex (*2*–*8*). One commonly proposed arrangement of metals in the active site is three closely spaced manganese centers, part of a heteronuclear Mn_3CaO_4 cubane, bridging via oxide or hydroxide ligands to a dangling fourth manganese (*2*–*9*). Given broad fundamental interest and potential applications in artificial photosynthesis, the structure of this cluster and the mechanism of water splitting to make dioxygen have been the subject of many spectroscopic, computational, synthetic, crystallographic, and biochemical studies (*1*, *10*–*12*). Despite major advances, the mechanism of oxygen production is not well understood. During one turnover, four oxidizing equivalents generated by light are delivered to the active-site cluster, leading to the stepwise formation of intermediates commonly referred to as the S states. The sequential transitions from S_0 (the most reduced state) to S_4 (the most oxidized state) involve electron- and proton-transfer events. The highly oxidized S_4 state is unstable and evolves dioxygen to return to the S_0 state. The exact Mn oxidation states and the site of O-O bond formation in S_4 are debated; nevertheless, high–oxidation state Mn centers are required to activate a terminal or bridging oxo ligand for O_2 production. The large protein matrix has complicated direct studies of the OEC active site, and the synthesis of small-molecule models has been impeded by the complexity of the cluster.

The synthesis of potentially biomimetic manganese oxide clusters has relied heavily on self-assembly because of the propensity of oxide and hydroxide ligands to bridge two or more metal centers (*13*). Judicious choice of ancillary ligands has enabled synthesis of a large variety of manganese clusters (*13*–*16*). Some of these complexes have provided valuable spectroscopic models for the OEC as well as insight into the reactivity of high–oxidation state manganese species, including water oxidation (*17*, *18*). The synthesis of an accurate model of the full active-site cluster has been elusive, however. Many di-, tri-, and tetranuclear clusters of manganese with bridging oxides have been reported (*16*), but incorporation of a calcium center is much less common (*19*–*24*). Although they incorporate a cuboidal arrangement, the reported Ca-Mn clusters are of much higher nuclearity than the OEC (*19*, *21*). Thus, fundamental studies on the role of calcium have been hindered by a lack of well-defined, small-molecule models.

To access heteronuclear clusters of predictable structure, we employed a recently developed trinucleating ligand framework. This architecture consists of a rigid 1,3,5-triarylbenzene spacer incorporating six pyridine and three alcohol groups (**1-H$_3$**, Fig. 1) (*25*, *26*). Reaction with three equivalents of manganese (II) acetate in the presence of base leads to the formation of a yellow trinuclear manganese complex, **2**, supported by pyridine donors and bridging alkoxides. Three capping acetates complete the coordination sphere of the metals. This trimetallic platform was envisioned as a precursor for the synthesis of more complex clusters.

Targeting a heterotetranuclear complex containing calcium and manganese, we treated **2** with two equivalents of potassium superoxide as a source of both oxygen atoms and oxidizing equivalents in the presence of $Ca(OTf)_2$ (OTf, trifluoromethanesulfonate) (Fig. 1). Although **2** is insoluble in tetrahydrofuran (THF), addition of $Ca(OTf)_2$ leads to partial dissolution of the suspended material, suggesting the formation of a more soluble Ca-Mn intermediate. Reaction with superoxide over 24 to 48 hours leads to the formation of a brown, heterogeneous mixture with a purple precipitate. Filtration affords a purple solid (**5**)—characterized by single-crystal x-ray diffraction (XRD) as a calcium-hexamanganese cluster in which two monooxygenated Mn_3 cores are linked to Ca^{2+} via acetate bridges (fig. S7)—and a brown supernatant. Vapor diffusion of hexane into the THF supernatant afforded red-brown crystals of compound **4**, which was also characterized by XRD. Compound **4** displays the desired $[Mn_3CaO_4]^{6+}$ core (Fig. 2, A and B). The three manganese centers are supported by framework **1**, with each manganese binding to one alkoxide and one pyridyl group; three pyridyl groups from **1** remain unbound. The manganese centers are pseudo-octahedral, and the calcium center is supported by three oxide ligands and three acetates that bridge across different faces of the cube. The calcium coordination sphere is completed by a THF molecule, consistent with a large heptacoordinate calcium center. Modeling all four metal sites as manganese centers does not fit the XRD data, and the Ca–O distances are all considerably longer than would be expected for Mn–O bonds (table S2). Analysis of the Mn-oxo distances in **4** reveals short average bond lengths of 1.87 Å, consistent with three Mn^{IV} centers. In agreement with this oxidation-state assignment, the standard deviation of the Mn-oxo bond lengths is small, as expected for a d^3 electronic configuration.

Department of Chemistry and Chemical Engineering, California Institute of Technology, 1200 East California Boulevard MC 127-72, Pasadena, CA 91125, USA.

*To whom correspondence should be addressed. E-mail: agapie@caltech.edu